Anomalous Above-Gap Photoexcitations and Optical Signatures of Localized Charge Puddles in Monolayer Molybdenum Disulfide

Nicholas J. Borys,*[†,‡] Edward S. Barnard,[†,‡] Shiyuan Gao,[§] Kaiyuan Yao,[†] Wei Bao,[†,‡,‖] Alexander Buyanin,[‡] Yingjie Zhang,[‡] Sefaattin Tongay,[‖,⊥] Changhyun Ko,[‖] Joonki Suh,[‖] Alexander Weber-Bargioni,[†,‡] Junqiao Wu,[‡,‖] Li Yang,[§] and P. James Schuck*[†,‡]

[†]Molecular Foundry, [‡]Materials Sciences Division, Lawrence Berkeley National Laboratory, Berkeley, California 94720, United States
[§]Department of Physics, Washington University in St. Louis, St. Louis, Missouri 63130, United States
[‖]Department of Materials Science and Engineering, University of California Berkeley, Berkeley, California 94720, United States
[⊥]Department of Materials Science and Engineering, Arizona State University, Tempe, Arizona 85287, United States

S Supporting Information

ABSTRACT: Broadband optoelectronics such as artificial light harvesting technologies necessitate efficient and, ideally, tunable coupling of excited states over a wide range of energies. In monolayer MoS_2, a prototypical two-dimensional layered semiconductor, the excited state manifold spans the visible electromagnetic spectrum and is comprised of an interconnected network of excitonic and free-carrier excitations. Here, photoluminescence excitation spectroscopy is used to reveal the energetic and spatial dependence of broadband excited state coupling to the ground-state luminescent excitons of monolayer MoS_2.

Photoexcitation of the direct band gap excitons is found to strengthen with increasing energy, demonstrating that interexcitonic coupling across the Brillouin zone is more efficient than previously reported, and thus bolstering the import and appeal of these materials for broadband optoelectronic applications. Narrow excitation resonances that are superimposed on the broadband photoexcitation spectrum are identified and coincide with the energetic positions of the higher-energy excitons and the electronic band gap as predicted by first-principles calculations. Identification of such features outlines a facile route to measure the optical and electronic band gaps and thus the exciton binding energy in the more sophisticated device architectures that are necessary for untangling the rich many-body phenomena and complex photophysics of these layered semiconductors. In as-grown materials, the excited states exhibit microscopic spatial variations that are characteristic of local carrier density fluctuations, similar to charge puddling phenomena in graphene. Such variations likely arise from substrate inhomogeneity and demonstrate the possibility to use substrate patterning to tune local carrier density and dynamically control excited states for designer optoelectronics.

KEYWORDS: transition metal dichalcogenides, monolayer molybdenum disulfide, broadband optical properties, exciton Stokes shift, localized carrier density, charge puddles
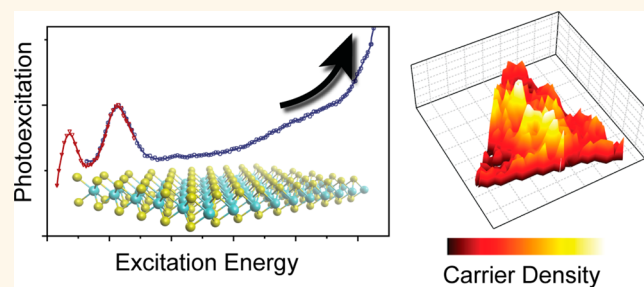
The field of two-dimensional (2D) optoelectronics has been revolutionized by the demonstrations[1−5] that monolayer (ML) transition metal dichalcogenides (TMDCs) form atomically thin direct band gap semiconductors, providing rich opportunities for both technological innovation and exploration of new physical phenomena.[6−12] Central to their optical and electronic properties is the enhanced Coulombic interaction that induces strong many-body effects such as the tightly bound exciton complexes which govern their resonant light-matter interactions.[13,14] Unlike traditional 2D semiconductor quantum wells, the excitons of

ML-TMDCs are stable at room temperature and under ambient conditions, liberating excitonic functionalities that were previously restricted to a cryogenic playground. Moreover, these exciton states exhibit strong sensitivity to the local electrostatic,[14] chemical[11] and structural[15,16] environment which simultaneously serves as a source of deleterious disorder

for macroscopic device applications yet provides facile means to locally probe[17] and manipulate[18] excitonic behavior.

Because of the large excitonic binding energy, multiple higher-energy bound states separate the lowest-energy exciton from free carrier interband excitations,[19] yielding a complex manifold of states that is important for broadband photo-physical applications.[20−22] Initial studies of these higher-energy states, including those using combined photoluminescence (PL) and scanning tunneling spectroscopy,[23] photocurrent excitation spectroscopy,[24] and photoluminescence excitation (PLE) spectroscopy,[20] provided some of the first evidence of the appreciably large exciton binding energy in ML-MoS$_2$. Additionally, PLE spectroscopy, where PL emission is measured as a function of excitation energy, has provided some initial insight into the complex relaxation and thermalization processes within the excited state manifold.[20,21] However, significant discrepancies in PLE intensities at higher energies—signatures of interexcitonic coupling across the Brillouin zone—exists between different studies and samples.[20,21] Furthermore, little is known about the spatial heterogeneity of these higher energy states. While rapid progress has been achieved in understanding the plethora of fascinating optoelectronic properties of the ground state excitons in ML-MoS$_2$ (and other TMDCs), much remains unknown, especially on a microscopic level, of the higher-energy states beyond the optical band gap despite their potential impact on applications ranging from solar cells[6] to quantum information science to 2D bioimaging[25,26] and sensing.[26]

In this work, we report the spectroscopic study and hyperspectral imaging of above-gap excitations in ML-MoS$_2$, enabled by a combination of PLE spectroscopy, DFT calculations, and microscopic PLE, PL and absorption spectroscopies. First, signatures of the Rydberg progression of the direct band gap excitons are observed, confirming the results of previous studies.[20,21] In contrast to these previous results, however, an "anomalous" increase in the photoexcitation of direct band gap excitons with increasing energy reveals efficient, broadband coupling pathways from higher-energy states to these photoemissive excitons. Within this increasing trend, additional features are resolved at energies that correspond to those of the electronic band gap as predicted by excited state density functional theory (DFT) calculations.[27] Second, the spatial heterogeneity of higher-energy states and their relaxation processes are investigated on a microscopic length scale using combined micro PL, PLE and absorption (μPL, μPLE and μAbsorption respectively) hyperspectral imaging. We find that the excitation resonances exhibit spatial heterogeneity that mimics that of the ground-state exciton energy, but not identically: the energetic Stokes shift between excitation and emission resonances, a metric for carrier density in ML-MoS$_2$,[14] is strikingly heterogeneous over individual flakes, providing all-optical evidence of spatial variations in local carrier density akin to charge puddles in graphene[28] and recently reported carrier-density variations in ML-MoSe$_2$.[29,30] Visualization of such perturbations to the excited state manifolds for these 2D systems is critical for developing future nanoscale TMDC technologies where tailoring local doping and excitonic properties are at the core of anticipated functionalities.

RESULTS AND DISCUSSION

Figure 1(a) shows the PLE spectrum of ML-MoS$_2$ grown by chemical vapor deposition on a SiO$_2$/Si substrate. The PLE
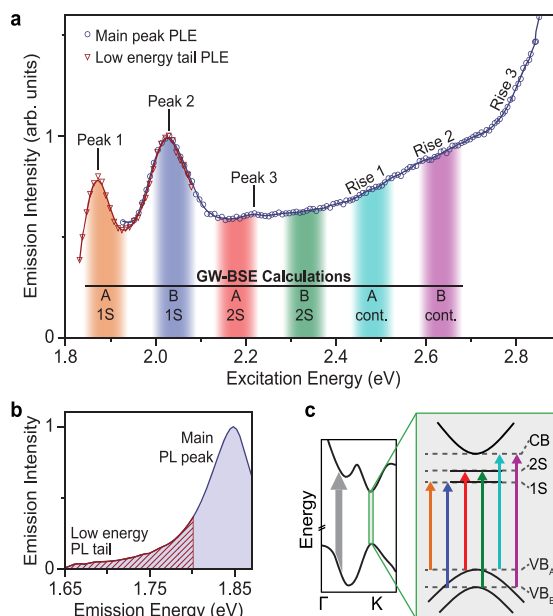
Figure 1. PLE spectroscopy of ML-MoS$_2$. (a) The PLE spectrum of a circular region with a radius of ~5 μm (~80 μm^2) of a single flake of ML-MoS$_2$ covering optical excitation from 1.82−2.87 eV. The data points are averages of up and down sweeps of excitation energy and the solid line is a smoothed guide to the eye. The prominent spectral features are labeled as Peaks 1−3 and Rises 1−3, and the overlaid colored columns beneath the data mark predicted energies of key optical transitions using GW−Bethe−Salpeter Equation calculations and estimated error bars. (b) The PL emission spectrum of ML-MoS$_2$ denoting the spectral regions of integration for the PLE measurement. (c) Schematic of the band-structure of ML-MoS$_2$ and the excitonic and free-carrier transitions at the K-point. The colored arrows denote the transitions reported in panel (a) and the large gray arrow marks the band nesting region of the Brillouin zone.

spectrum was acquired by integrating the PL emission (Figure 1(b)) as a function of excitation energy over the range of 1.82−2.87 eV from a large area (~10 μm in diameter) of a single flake. Utmost care was taken to ensure our measurements were performed in the linear excitation regime, appropriately corrected for a constant flux of photons and external quantum efficiency factors (such as thin-film interference of the excitation radiation; see SI Figure S1), and conducted sufficiently fast to minimize photodegradation effects that can particularly afflict the measurement at higher excitation energies (see SI Figure S2). For excitation energies above 1.92 eV, the PL was integrated over the main exciton A peak (from 1.65 to 1.88 eV), but at lesser excitation energies, the emission energy range was restricted to the low-energy tail of the PL (from 1.65 to 1.82 eV) in order to avoid the spectral overlap between the PL and the laser excitation. To adjust for the intensity difference between the two spectral ranges, the low-energy PLE spectrum (red curve) is scaled to align with the high-energy PLE spectrum (blue curve) at ~2.1 eV. In this manner, excited states that are near the optical band gap can be resolved and indeed, the two most pronounced excitation resonances are observed at 1.88 eV (Peak 1) and 2.03 eV (Peak 2), in agreement with the typical absorption spectrum of ML-MoS$_2$[1] (see SI Figure S3). Beyond these lowest-energy resonances, the absorption spectrum is generally featureless, but the PLE spectrum exhibits a small resonant peak at 2.22 eV (Peak 3) on

top of a broadband continuum-like background. As discussed below, this background obscures identification of additional peak-like features at higher energies. However, at 2.48 eV, the PLE spectrum exhibits an onset-like increase in slope (Rise 1) which then decreases at 2.62 eV (Rise 2) before dramatically increasing at ∼2.75 eV (Rise 3)—features that were not identified in previous PLE studies.[20,21] Signatures of all of these features are also identifiable in the first derivative of the PLE spectrum (see SI Figure S4), and we note that these six spectral features were consistent over numerous flakes of ML-MoS₂. For different samples, the more subtle features of Peak 3, Rise 1 and Rise 2 were difficult to identify in those with lower PL quantum yields, but the general trend of strengthening photoexcitation with increasing excitation energy was observed in all ML-MoS₂ samples investigated regardless of the substrate material (i.e., SiO₂/Si or sapphire; see SI Figures S1, S3 and S4).

For a 2D quantum well with noninteracting electrons, the PLE spectrum should exhibit a single step at the energy of the band gap.[19,31] With strong electron−hole interactions (as is the case for ML-MoS₂), sub-band gap excitons emerge and the oscillator strength of the band-to-band transition is "shifted" into the bound states.[19,31,32] The excitation spectrum is then expected to be a progression of weakening exciton absorption resonances that merge into a broadened, step-like onset of interband transitions[19,31] at the quasiparticle band gap (i.e., the transport or electronic band gap). For ML-MoS₂, the direct band gap occurs at the K-point in the Brillouin zone where spin−orbit coupling splits the valence bands by ∼150 meV, giving rise to two energetically separated manifolds of such states, commonly referred to as the A and B excitons (Figure 1(c)). First-principle excited state calculations were used to estimate the energies of these excitonic and free-carrier optical resonances for the A and B manifolds. The calculated energy of each transition is overlaid in Figure 1(a) as a shaded vertical column, where the 100 meV width reflects the uncertainty in the predictions. For the 1S states of the A and B excitons, the calculated energies are respectively centered on 1.89 eV (orange column) and 2.04 eV (blue column) while the respective 2S states are predicted to lie at 2.18 eV (red column) and 2.33 eV (green column). Beyond the exciton resonances, the onsets of continuum absorption of free-carrier excitations at the quasiparticle band gap are predicted by DFT to occur at 2.48 eV (teal column) and 2.63 eV (purple column) for the A and B excitons, respectively.

At energies below 2.75 eV, each primary feature of the PLE spectrum coincides with a predicted state from the DFT calculations. The changes in slope at 2.48 and 2.62 eV (Rises 1 and 2, respectively) are near the predicted energies of the quasiparticle band gap on a SiO₂ substrate. Given this agreement, we hypothesize that these features are related to the A, and potentially the B, quasiparticle (i.e., electronic) band gaps. Our results and assignments are supported by photocurrent excitation measurements,[24] which observe a similar feature at 2.5 eV. Due to broadening and convolution with other states, we suspect that the anticipated step-like feature of continuum absorption is blurred into these more subtle changes of slope and note that more clear spectral features might be obtainable under cryogenic conditions. The correspondence between the excited state calculations and the PLE spectrum alone does not offer conclusive proof that these features correspond to the quasiparticle band gap but is nevertheless encouraging and motivates future studies that, for example,

employ electrostatic gating where renormalization effects[33] can be employed to confirm our hypothesis.

For the excitonic transitions, the lowest energy resonances in the PLE spectrum (Peaks 1 and 2) agree remarkably well with the calculated energies for the 1S states of the A and B excitons. However, only a resonant peak for the 2S state of the A exciton is observed at 2.22 eV (Peak 3), whereas no such peak is resolved for that of the B exciton. Discerning the weaker higher-energy exciton states from the broadband background can be limited by broadening of the optical transition. The PLE spectrum here as well as previous steady-state[1] and transient[34,35] absorption studies indicate that the linewidth of the B exciton is ∼1.5× larger than that of A exciton (see SI Figure S6). Summarizing a more detailed discussion on the role of broadening in the PLE spectrum (see SI Figure S7 and accompanying discussion), it is quite possible that the broader 2S state of exciton B cannot be discerned from the background. This same issue regarding the assignment of Peak 3 was treated by Hill et al.[20] who inferred an exciton binding energy of 0.44 eV by assigning it to exciton B or 0.64 eV if it is assigned to exciton A. In our case, the energetic separation between the onset-like feature (Rise 1; 2.48 eV)—which we tentatively assign to the quasiparticle band gap—and the 1S state of exciton A (Peak 1; 1.88 eV) provides an estimate of the exciton binding energy of ∼600 meV (at the intrinsic n-type carrier density present in these flakes), which agrees with the latter prediction of Hill et al.[20] when Peak 3 is assigned to exciton A. Furthermore, the assignment of Rise 1 to the quasiparticle band gap of the exciton A manifold of states agrees with the band gap value determined by Klots et al.[24] using photocurrent excitation spectroscopy. Taking the excited state calculations and previous studies into account, the spectral features identified here indicate that the exciton binding energy in the samples used in this work is ∼600 meV.

In addition to the exciton states, the PLE spectrum generally exhibits increasing photoexcitation strength with increasing excitation energy, which is anomalous for a conventional 2D quantum well as discussed above. At higher photon energies, strong optical absorption occurs from transitions in the band-nesting region between the sigma and gamma points of the Brillouin zone (Figure 1(c)).[19,21,24,36] We attribute this anomalous increase in photoexcitation to coupling of the excitations in the band-nesting region to the direct band gap excitons at the K-point in the Brillouin zone. In contrast, previous measurements[20,21] reported a decrease in the PLE spectrum at these higher energies (see SI Figure S5), concluding minimal coupling of the two excitation manifolds. While this increasing trend was ubiquitous in all of the samples investigated here regardless of the substrate, variations in sample quality remain as a possible origin of these discrepancies between our results and these previous studies and warrant a more focused investigation that directly compares different samples of known relative quality as well as samples with differing carrier localization and scattering centers. Regardless, our results clearly demonstrate that direct band gap excitons can be efficiently generated over a broadband spectral range and that photoexcitation is not limited to the excitations at the K-point in the Brillouin zone and can in fact, be more efficient at higher excitation energies.

Single flakes of ML-MoS₂ are known to have excitonic properties that are spatially inhomogeneous, and PLE spectroscopy that averages over large areas as in Figure 1 misses important spatial variations in optoelectronic properties in

analogy to the contrast between ensemble and single molecule spectroscopies.[37] Exemplifying this point, Figure 2 shows two
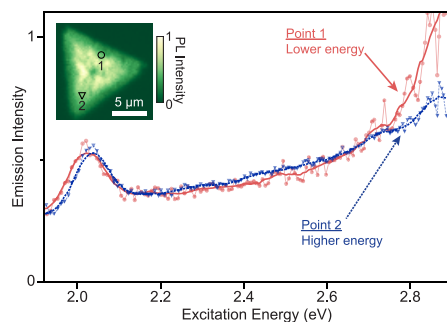

Figure 2. Spatial inhomogeneity and disorder broadening of PLE spectra of a single-flake of ML-MoS₂. Two μPLE measurements are shown from circular regions with radii of $\sim$500 nm ($\sim$0.8 μm^2) at the spatially distinct points denoted in the inset μPL image of the flake. Again, the data points are averages of up and down sweeps in the excitation energy and the solid lines are smoothed guides to the eye. The smaller amount of probed material reduces the signal-to-noise ratio of the spectra, but shifts of the 1S state of the B exciton and anomalous excitation feature to higher energies from Point 1 to Point 2 are resolvable. The same energetic shift is also observed in the PL spectra of the two points as shown in the SI.

individual μPLE spectra acquired from spatially distinct regions of a single flake of ML-MoS₂ with a spatial resolution of $\sim$1 μm. Because the higher-resolution illumination area is $\sim$100$\times$ smaller than that of Figure 1, the signal-to-noise ratios of the μPLE spectra are reduced, but the 1S state of exciton B is still clearly resolvable and it is easy to discern that this excitation resonance is $\sim$20 meV lower in energy at Point 1 than at Point 2. Similarly, the anomalous absorption feature is also at a lower energy at Point 1, and in terms of PL, this energetic shift is also observed in the emission from the lowest-energy exciton A state (see SI Figure S8). Such spatial heterogeneity of ground-state exciton energy, population and relaxation kinetics can result from localized strain,[15,16] grain boundaries,[38] chemical composition,[17,39] carrier density[14,17,40] and dielectric screening.[41] In analogy to μPL microscopy, hyperspectral μPLE imaging (i.e., PLE spectroscopy at discrete locations to form a hyperspectral image) can characterize the spatial dispersion and relative amount of disorder of the higher-energy excited states. And further, having simultaneous access to the local energies of the ground state exciton emission and the higher-lying excitation resonances provides an opportunity to microscopically trace local relaxation processes between excited states.

Hyperspectral μPLE imaging of a single flake of ML-MoS₂ is shown in Figure 3. The local μPL and μPLE spectra of the single flake are mapped with a resolution of $\sim$1 μm. The energetic range of the μPLE spectroscopy was focused on the 1S resonance of the B exciton. The μPL (red data sets) and μPLE (blue data sets) spectra of two distinct points are shown in Figure 3(a) and confirm the observed heterogeneity in Figure 2. From each spatial position, the energy of the PL emission from the 1S state of the A exciton ($E_{A,PL}$) and the energy of the excitation resonance of the 1S state of the B exciton ($E_{B,PLE}$) can be extracted from the PL and PLE spectra, respectively. Spatial maps of $E_{A,PL}$ and $E_{B,PLE}$ and are shown alongside each other in Figures 3(b) and 3(c), respectively. The two maps exhibit a strong spatial correlation between high- and low-energy regions: variations in the *emission* energy of exciton
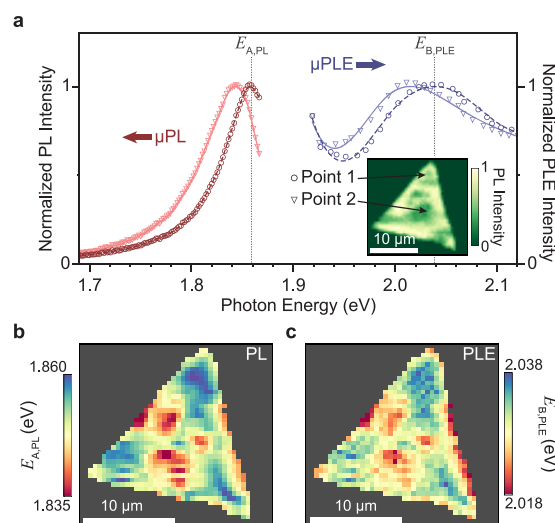

Figure 3. Imaging of the spatial disorder of the emission and excitation resonances of excitons in a single flake of ML-MoS₂. (a) Sample μPL (red data sets) and μPLE (blue data sets) spectra from $\sim$0.8 μm^2 regions at two distinct points of a single flake of ML-MoS₂ (μPL map inset). The PLE measurement spans only the energetic region of the 1S state of the B exciton (due to time constraints). The PLE data points are averaged over up and down sweeps of excitation energy while the PL spectra are averaged over all excitation energies. For all curves, the solid lines serve a guide to the eye. From the μPL and μPLE data sets, the energies of the emission resonance of the 1S state of exciton A ($E_{A,PL}$) and the excitation resonance of the 1S state of exciton B ($E_{B,PLE}$) are extracted at each point and mapped in (b) and (c), respectively.

A ($E_{A,PL}$) are mimicked in the *absorption/excitation* energy of exciton B ($E_{B,PLE}$). Indeed, it is not overly surprising that material and environmental variations that, for example, alter the local Coulombic screening between the electron and hole similarly affect the A and B exciton states. However, close inspection reveals that the spatial variations of these resonance energies are not identical and that the energetic separation between the excitation and emission resonances, or in other words, the amount of energy thermalized during relaxation from the B to the A exciton states, changes from one spatial position to the next.

Figure 4 shows the spatial variations of the amount of energy deposited into the ML-MoS₂ as the higher-energy B excitons relax to the lowest energy A excitons for the single flake in Figure 3. The energetic separation between the emission and excitation resonances ($\Delta E = E_{B,PLE} - E_{A,PL}$), is heterogeneous and marked by distinct regions of larger and smaller energetic separations (Figures 4(a) and 4(b)). We further find that the spatial heterogeneity of the ΔE is strongly correlated to the energy of the excitonic states themselves as shown in Figure 4c. As the emission shifts to lower energies, the amount of energy thermalized as the higher-energy B excitons relax to the ground state A exciton increases. Unfortunately, it is difficult to understand this correlated relationship in greater detail because with these particular excitation and emission resonances, ΔE is composed of the sum of the spin−orbit splitting between the valence bands ($\Delta E_{spin-orbit}$) and the excitonic Stokes shift (ΔE_{Stokes}) which is defined as the difference between the energetic positions of excitation and emission resonances of the 1S state of the A exciton.
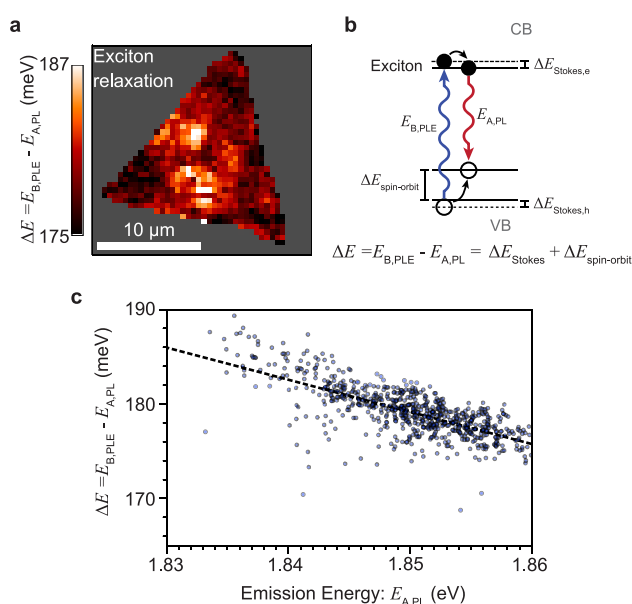
Figure 4. Spatial mapping of relaxation energetics of a single flake of ML-MoS$_2$. (a) Spatial dispersion of the amount of energy thermalized upon excitation of higher-energy B excitons which relax to the lowest energy, photoemissive A exciton. (b) Schematic of the relationship between the relaxation energy reported in (a) to the spin−orbit coupling and Stokes shift quantities. The overall Stokes shift (ΔE_{Stokes}) is the sum of the Stokes shift for the hole ($\Delta E_{\text{Stokes,h}}$) and for the electron ($\Delta E_{\text{Stokes,e}}$). (c) Correlation plot between the relaxation energies in panel (a) with the local emission energies (Figure 3b). The dashed line is a fit to the data set, qualitatively showing the linear nature of the correlation.

Disentangling the spin−orbit splitting ($\Delta E_{\text{spin−orbit}}$) from the excitonic Stokes shift (ΔE_{Stokes}) is critical to understanding the origins of the spatially heterogeneous excited state relaxation (Figure 4), and such a task necessitates also probing the local energy of the excitation resonance of the A exciton itself. Thus, the ideal approach would be to extend the μPLE measurements to lower energies by monitoring only the tail of the PL emission as in Figure 1. In our experimental setup, this approach required excessively long integration times that prohibited drift-free, macroscopic imaging. As an alternative, we performed hyperspectral μAbsorption and μPL imaging of a single flake of ML-MoS$_2$, acquiring the local absorption and PL spectra with a spatial resolution of ∼500 nm, the results of which are shown in Figure 5. With this data set, the energies of the PL (Figure 5a), and the A and B absorption resonances (Figure 5b) are mapped over the extent of a single flake and reveal distinct regions of higher and lower excitonic energies. Whereas the PL spectra are analyzed by straightforward peak fitting routines, the μAbsorption spectra must be calculated using Kramers−Kronig analysis of the broadband reflectance spectra (see SI Figure S9 and associated discussion for details). From these calculated absorption spectra, the local spin−orbit splitting is determined by the energetic separation of the A and B exciton resonances and is found to be relatively homogeneous over the flake with the exception of a few pronounced regions of lower energies (Figure 5c). In contrast, the Stokes shift determined from the energetic separation of the emission and absorption resonances of the A exciton, is significantly more inhomogeneous over the flake (Figure 5d). This heterogeneity is readily apparent by comparing the optical spectra at different spectral locations as seen in Figure 5e. Lastly, Figure 6 reports the statistical correlations between the local exciton energy with the Stokes shift and spin−orbit splitting values of the flake in Figure 5. Whereas the spatial heterogeneity of the spin−orbit splitting is
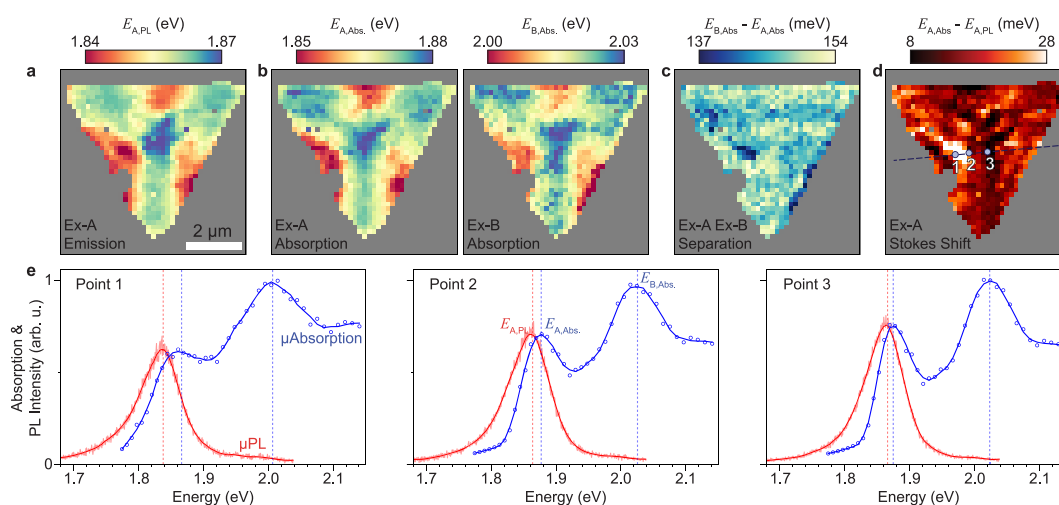
Figure 5. Hyperspectral μPL and μAbsorption imaging of the excitonic emission and absorption resonances of a single flake of ML-MoS$_2$. (a) The emission energy at each position was determined by peak fitting analysis of the PL spectrum (see SI for details). (b) The energies of the exciton A and B excitation resonances were extracted from absorption spectra calculated by Kramers−Kronig analysis of broadband reflectance spectra acquired at each point (see SI for details). Both absorption resonances show the same general regions of a high and low energies as the emission. (c) The separation between the A and B absorption resonances as derived from the μAbsorption data in panel (b) is more homogeneous but distinct regions of smaller separations are observed. (d) In contrast, the excitonic Stokes shift between the emission and lowest energy absorption resonance is heterogeneous over the flake exhibiting several clear microscopic regions of lower and higher values. (e) μPL and μAbsorption spectra at the specific points 1, 2, and 3 marked in panel (d) exemplify the spatial variations of the excitation and emission resonances and the resulting variations in the excitonic Stokes shift. An ∼750 nm edge region around the flake is excluded from the analysis because scattering effects at the edge prohibit unambiguous Kramers−Kronig analysis in these regions.
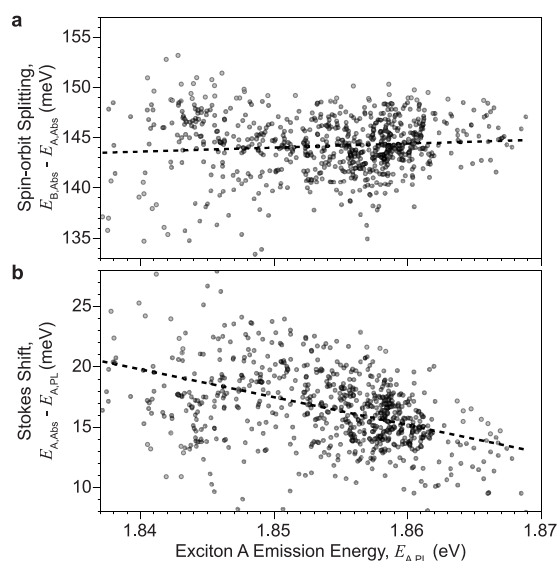
Figure 6. Relationships between the excitonic Stokes shift and energetic separation of the exciton A and B absorption resonances with the energy of the excitonic PL. (a) The separation between the A and B excitation resonances in the absorption spectrum is found to be largely uncorrelated to the emission energy of the exciton. The dashed line is a linear fit to the data, showing that spin−orbit splitting is not strongly correlated to the exciton energy. (b) In contrast, the Stokes shift between the emission and absorption resonances of the A exciton is correlated with energy of the exciton state. Again, the dashed line is a linear fit to the data, showing the correlation of the Stokes shift with the exciton energy is much stronger than the spin−orbit splitting. The statistical scatter in both panels is attributed to the uncertainty in the complex process of determining the exciton absorption resonances from the reflectance spectra.

largely independent of the exciton energy (Figure 6a), the excitonic Stokes shifts (Figure 6b) exhibits nearly the same correlation as observed in μPLE measurements that are reported in Figure 4c. Spatial regions of lower exciton energies tend to exhibit larger Stokes shifts. We therefore conclude that the observed variations in exciton relaxation energies (*i.e.*, ΔE in Figure 4) arise predominantly from spatial variations in the excitonic Stokes shift.

For semiconductor quantum wells, a Stokes shift arises from disorder-induced exciton localization caused by inhomogeneous quantum well widths or alloying.[42−44] This defect-based interpretation has been extended to a Stokes shift between resonance Raman scattering and PL of ML-MoS$_2$.[45] However, it is unclear why such disorder effects would be so inhomogeneously distributed over a single flake as seen here. Alternatively, a Stokes shift can also arise due to carrier doping in ML-MoS$_2$[14] as state-filling in the conduction band can prevent direct excitation of the lowest-energy excitons[14,46] (*i.e.*, absorption energy increases due to band filling/Pauli blocking; Figure 4(b)). Indeed, from the PL energy, which is low compared to what is reported for undoped ML-MoS$_2$, we infer that our samples are substantially n-doped and that the excitonic resonances are dominated more specifically by trions.[14] As seen in Figures 4c and 6b, the local Stokes shift for both the A and B excitation resonances correlates with the local energy of the PL: regions with higher energy excitons have smaller Stokes shifts. A similar trend was reported by Mak *et al.*[14] where electrostatic gating was utilized to systematically

change the carrier density. Increasing carrier concentration was found to increase the Stokes shift and decrease the energy of the PL. A direct comparison of the data in the heavy doping regime from this previous study[14] to the spatial variations seen here reveals remarkable agreement (see SI Figure S10). We therefore deduce that the spatial heterogeneity of the energies of the exciton states largely manifests from local variations in carrier density, in analogy to substrate-induced charge puddles in graphene.[28]

Initial evidence for such charge puddling phenomena was found in hyperspectral nano-PL microscopy that resolved nanoscale variations in the relative populations of excitons and trions in ML-MoS$_2$[17] as well as in hyperspectral four-wave mixing microscopy[29] and transient pump−probe spectroscopy of ML-MoSe$_2$.[30] We additionally attempted to correlate these optical signatures of carrier density variations to fluctuations of the surface potential using scanning Kelvin probe force microscopy (see SI Figure S11). These preliminary measurements revealed spatial fluctuations of the surface potential across the single flake of ML-MoS$_2$, but require a more detailed study to fully account for effects of water layers and surface contamination. And finally, recent theoretical work[47] suggests that such carrier density variations may coincide with spatially dependent band gap renormalization, possibly resulting from inhomogeneous strain induced by the growth process (see SI Figure S12). Such local strain effects have been observed for the exciton energies in ML-WSe$_2$ using precise optical nanospectroscopy[48] and motivates future μPLE imaging that is optimized to precisely extract the local energy of the quasiparticle band gap.

CONCLUSIONS

In summary, PLE spectroscopy and spectroscopic imaging provide simple yet powerful means to investigate the rich manifold of excited states of ML-TMDC semiconductors over a broad range of excitation energies beyond the optical band gap. Contrary to previous PLE studies,[20,21] an *increase* in excitation of the direct band gap excitons with increasing excitation energy is observed, likely arising from efficient relaxation of higher-energy excitations across the Brillouin zone and demonstrating the potential of using the direct band gap exciton states of ML-MoS$_2$ and other TMDC semiconductors in broadband optoelectronic devices. Narrow resonant peaks and subtle onset features in the photoexcitation spectrum are also identified with energetic positions that are aligned with the states of the Rydberg progression of the A and B excitons as well as their respective quasiparticle band gaps, as predicted by first-principles excited state calculations. The latter spectral features, if proven to correspond to the quasiparticle band gap *via*, for example, gating measurements, provide explicit means to quantify the quasiparticle band gap and thus exciton binding energy in a wide-variety of device configurations for ML-TMDC semiconductors. Microscopically, combined hyperspectral μPLE, μPL and μAbsorption imaging shows that the higher-energy excitation resonances exhibit spatial disorder that mimics that of the ground-state exciton, but not perfectly: local variations in the Stokes shifts between the excitonic absorption and emission resonances are revealed and exhibit behavior that is indicative of variations arising from spatial fluctuations in carrier densities in analogy to charge puddles in graphene. Almost certainly, 2D ML-TMDC semiconductors will play a central role in ultrathin, flexible optoelectronic technologies, necessitating a precise understanding of such excited states

beyond the ground-state exciton and the corresponding coupling pathways to fully optimize performance.

EXPERIMENTAL METHODS

Optical Spectroscopy. Wide area illumination ∼10 μm in diameter (Figure 1) or focused illumination 500 nm −1 μm in diameter (Figures 2−4) of 2.5 nm wide spectral bands of a white light supercontinuum laser (Luekos; 5 ps pulses at a 40 MHz repetition rate, spectrally isolated with a Gooch and Housego AOTF) were systematically scanned to excite the PL over up and down sweeps, recording a full emission spectrum at each point on a cooled charged-coupled device (Andor iXon EMCCD) attached to a spectrometer (Acton 2300i). For all excitation energies, the excitation density was kept in the range in which the PL scales linearly with excitation density (less than 100 W/cm^2 CW-equivalent at 620 nm). Excitation light from the AOTF was further filtered by short-pass filters (ET650SP, Thorlabs & 3G LVSWP, Delta Optical Thin Films), and at each excitation energy, the laser spectrum and power were recorded on a fiber optic spectrometer (OceanOptics) and photodiode (Thorlabs). Before the spectrometer, laser light was filtered from the PL using multiple interference filters (HQ710/100, Semrock & 3G LVLWP, Delta Linear Optical Thin Films) resulting in a transmission band from 660 to 750 nm. For excitation energies lower than 1.92 eV, the transmission band was adjusted to a lower energy region from 690 to 750 nm. PLE intensity was calculated by integrating the emission spectrum at each energy and corrected for variations in laser power so that the intensity is reported for a constant flux of photons. PL intensity maps were recorded at an excitation wavelength of 530 nm (2.33 eV) using the same microscope as the PLE measurements but with a single-photon avalanche photodiode (MPD) for the detector. The absorption spectroscopy measurements were performed by recording the reflectance spectra from a broadband lamp at normal incidence to the sample. Spatial resolution was achieved using a pinhole with a size corresponding to a circular area with a diameter of 400 nm on the sample. Absorption spectra were calculated using restrained Kramers−Kronig analysis as described in previous work.[14] All measurements were conducted at ambient conditions.

Sample Growth. A complete description of the growth procedure is provided in a previous publication.[17]

Excited State Calculations. The ground-state properties are calculated by Density Functional Theory (DFT) with the Perdew, Burke and Ernzerhof (PBE) functional,[49] using the Quantum Espresso.[50] The quasiparticle band gap is obtained by the single-shot G_0W_0 calculation with the general plasmon-pole (GPP) approximation.[51] The excitonic effects are included by solving the Bethe−Salpeter Equation (BSE).[52] The coarse k-point grid for the electron−hole interaction kernel is 24 × 24 × 1 and it is interpolated to a finer k-grid of 60 × 60 × 1 for obtaining converged excitonic states.[19,27] The GW-BSE calculation is done with the BerkeleyGW package.[53] The effect of temperature is included by considering the lattice expansion.[27]

ASSOCIATED CONTENT

Ⓢ Supporting Information

The Supporting Information is available free of charge on the ACS Publications website at DOI: 10.1021/acsnano.6b08278.

Additional data on the effects of photodegredation, thin film interference effects, broadening, strain, and carrier density (PDF)

AUTHOR INFORMATION

Corresponding Authors

*E-mail: njborys@lbl.gov.
*E-mail: pjschuck@lbl.gov.

ORCID Ⓞ

Nicholas J. Borys: 0000-0001-5434-1191

REFERENCES

(1) Mak, K. F.; Lee, C.; Hone, J.; Shan, J.; Heinz, T. F. Atomically Thin Mos$_2$: A New Direct-Gap Semiconductor. *Phys. Rev. Lett.* **2010**, *105*, 136805.

(2) Splendiani, A.; Sun, L.; Zhang, Y.; Li, T.; Kim, J.; Chim, C.-Y.; Galli, G.; Wang, F. Emerging Photoluminescence in Monolayer MoS$_2$. *Nano Lett.* **2010**, *10*, 1271−1275.

(3) Tonndorf, P.; Schmidt, R.; Boettger, P.; Zhang, X.; Boerner, J.; Liebig, A.; Albrecht, M.; Kloc, C.; Gordan, O.; Zahn, D. R. T.; de Vasconcellos, S. M.; Bratschitsch, R. Photoluminescence Emission and Raman Response of Monolayer MoS$_2$, MoSe$_2$, and WSe$_2$. *Opt. Express* **2013**, *21*, 4908−4916.

(4) Zeng, H.; Liu, G.-B.; Dai, J.; Yan, Y.; Zhu, B.; He, R.; Xie, L.; Xu, S.; Chen, X.; Yao, W.; Cui, X. Optical Signature of Symmetry Variations and Spin-Valley Coupling in Atomically Thin Tungsten Dichalcogenides. *Sci. Rep.* **2013**, *3*, 1608.

(5) Zhao, W.; Ghorannevis, Z.; Chu, L.; Toh, M.; Kloc, C.; Tan, P.-H.; Eda, G. Evolution of Electronic Structure in Atomically Thin Sheets of WS$_2$ and WSe$_2$. *ACS Nano* **2013**, *7*, 791−797.

(6) Wang, Q. H.; Kalantar-Zadeh, K.; Kis, A.; Coleman, J. N.; Strano, M. S. Electronics and Optoelectronics of Two-Dimensional Transition Metal Dichalcogenides. *Nat. Nanotechnol.* **2012**, *7*, 699−712.

(7) Radisavljevic, B.; Radenovic, A.; Brivio, J.; Giacometti, V.; Kis, A. Single-Layer MoS$_2$ Transistors. *Nat. Nanotechnol.* **2011**, *6*, 147−150.

(8) Lopez-Sanchez, O.; Lembke, D.; Kayci, M.; Radenovic, A.; Kis, A. Ultrasensitive Photodetectors Based on Monolayer MoS$_2$. *Nat. Nanotechnol.* **2013**, *8*, 497−501.

(9) Sundaram, R. S.; Engel, M.; Lombardo, A.; Krupke, R.; Ferrari, A. C.; Avouris, P.; Steiner, M. Electroluminescence in Single Layer MoS$_2$. *Nano Lett.* **2013**, *13*, 1416−1421.

(10) Perkins, F. K.; Friedman, A. L.; Cobas, E.; Campbell, P. M.; Jernigan, G. G.; Jonker, B. T. Chemical Vapor Sensing with Monolayer MoS$_2$. *Nano Lett.* **2013**, *13*, 668−673.

(11) Tongay, S.; Zhou, J.; Ataca, C.; Liu, J.; Kang, J. S.; Matthews, T. S.; You, L.; Li, J.; Grossman, J. C.; Wu, J. Broad-Range Modulation of Light Emission in Two-Dimensional Semiconductors by Molecular Physisorption Gating. *Nano Lett.* **2013**, *13*, 2831−2836.

(12) Britnell, L.; Ribeiro, R. M.; Eckmann, A.; Jalil, R.; Belle, B. D.; Mishchenko, A.; Kim, Y. J.; Gorbachev, R. V.; Georgiou, T.; Morozov, S. V.; Grigorenko, A. N.; Geim, A. K.; Casiraghi, C.; Castro Neto, A. H.; Novoselov, K. S. Strong Light-Matter Interactions in Hetero-structures of Atomically Thin Films. *Science* **2013**, *340*, 1311−1314.

(13) He, K.; Kumar, N.; Zhao, L.; Wang, Z.; Mak, K. F.; Zhao, H.; Shan, J. Tightly Bound Excitons in Monolayer WSe$_2$. *Phys. Rev. Lett.* **2014**, *113*, 026803.

(14) Mak, K. F.; He, K.; Lee, C.; Lee, G. H.; Hone, J.; Heinz, T. F.; Shan, J. Tightly Bound Trions in Monolayer MoS$_2$. *Nat. Mater.* **2013**, *12*, 207−211.

(15) Liu, Z.; Amani, M.; Najmaei, S.; Xu, Q.; Zou, X.; Zhou, W.; Yu, T.; Qiu, C.; Birdwell, A. G.; Crowne, F. J.; Vajtai, R.; Yakobson, B. I.; Xia, Z.; Dubey, M.; Ajayan, P. M.; Lou, J. Strain and Structure

Heterogeneity in MoS$_2$ Atomic Layers Grown by Chemical Vapour Deposition. *Nat. Commun.* **2014**, *5*, 5246.

(16) Yang, L.; Cui, X.; Zhang, J.; Wang, K.; Shen, M.; Zeng, S.; Dayeh, S. A.; Feng, L.; Xiang, B. Lattice Strain Effects on the Optical Properties of MoS$_2$ Nanosheets. *Sci. Rep.* **2014**, *4*, 5649.

(17) Bao, W.; Borys, N. J.; Ko, C.; Suh, J.; Fan, W.; Thron, A.; Zhang, Y.; Buyanin, A.; Zhang, J.; Cabrini, S.; Ashby, P. D.; Weber-Bargioni, A.; Tongay, S.; Aloni, S.; Ogletree, D. F.; Wu, J.; Salmeron, M. B.; Schuck, P. J. Visualizing Nanoscale Excitonic Relaxation Properties of Disordered Edges and Grain Boundaries in Monolayer Molybdenum Disulfide. *Nat. Commun.* **2015**, *6*, 7993.

(18) Li, H.; Contryman, A. W.; Qian, X. F.; Ardakani, S. M.; Gong, Y. J.; Wang, X. L.; Weisse, J. M.; Lee, C. H.; Zhao, J. H.; Ajayan, P. M.; Li, J.; Manoharan, H. C.; Zheng, X. L. Optoelectronic Crystal of Artificial Atoms in Strain-Textured Molybdenum Disulphide. *Nat. Commun.* **2015**, *6*, 7381.

(19) Qiu, D. Y.; da Jornada, F. H.; Louie, S. G. Optical Spectrum of MoS$_2$: Many-Body Effects and Diversity of Exciton States. *Phys. Rev. Lett.* **2013**, *111*, 216805.

(20) Hill, H. M.; Rigosi, A. F.; Roquelet, C.; Chernikov, A.; Berkelbach, T. C.; Reichman, D. R.; Hybertsen, M. S.; Brus, L. E.; Heinz, T. F. Observation of Excitonic Rydberg States in Monolayer MoS$_2$ and WS$_2$ by Photoluminescence Excitation Spectroscopy. *Nano Lett.* **2015**, *15*, 2992−2997.

(21) Kozawa, D.; Kumar, R.; Carvalho, A.; Amara, K. K.; Zhao, W.; Wang, S.; Toh, M.; Ribeiro, R. M.; Castro Neto, A. H.; Matsuda, K.; Eda, G. Photocarrier Relaxation Pathway in Two-Dimensional Semiconducting Transition Metal Dichalcogenides. *Nat. Commun.* **2014**, *5*, 4543.

(22) Steinhoff, A.; Kim, J. H.; Jahnke, F.; Rösner, M.; Kim, D. S.; Lee, C.; Han, G. H.; Jeong, M. S.; Wehling, T. O.; Gies, C. Efficient Excitonic Photoluminescence in Direct and Indirect Band Gap Monolayer MoS$_2$. *Nano Lett.* **2015**, *15*, 6841−6847.

(23) Zhang, C.; Johnson, A.; Hsu, C.-L.; Li, L.-J.; Shih, C.-K. Direct Imaging of Band Profile in Single Layer MoS$_2$ on Graphite: Quasiparticle Energy Gap, Metallic Edge States, and Edge Band Bending. *Nano Lett.* **2014**, *14*, 2443−2447.

(24) Klots, A. R.; Newaz, A. K. M.; Wang, B.; Prasai, D.; Krzyzanowska, H.; Lin, J. H.; Caudel, D.; Ghimire, N. J.; Yan, J.; Ivanov, B. L.; Velizhanin, K. A.; Burger, A.; Mandrus, D. G.; Tolk, N. H.; Pantelides, S. T.; Bolotin, K. I. Probing Excitonic States in Suspended Two-Dimensional Semiconductors by Photocurrent Spectroscopy. *Sci. Rep.* **2014**, *4*, 6608.

(25) Hall, L. T.; Beart, G. C. G.; Thomas, E. A.; Simpson, D. A.; McGuinness, L. P.; Cole, J. H.; Manton, J. H.; Scholten, R. E.; Jelezko, F.; Wrachtrup, J.; Petrou, S.; Hollenberg, L. C. L. High Spatial and Temporal Resolution Wide-Field Imaging of Neuron Activity Using Quantum NV-Diamond. *Sci. Rep.* **2012**, *2*, 401.

(26) Sarkar, D.; Liu, W.; Xie, X. J.; Anselmo, A. C.; Mitragotri, S.; Banerjee, K. MoS$_2$ Field-Effect Transistor for Next-Generation Label-Free Biosensors. *ACS Nano* **2014**, *8*, 3992−4003.

(27) Soklaski, R.; Liang, Y.; Yang, L. Temperature Effect on Optical Spectra of Monolayer Molybdenum Disulfide. *Appl. Phys. Lett.* **2014**, *104*, 193110−193110.

(28) Zhang, Y. B.; Brar, V. W.; Girit, C.; Zettl, A.; Crommie, M. F. Origin of Spatial Charge Inhomogeneity in Graphene. *Nat. Phys.* **2009**, *5*, 722−726.

(29) Jakubczyk, T.; Delmonte, V.; Koperski, M.; Nogajewski, K.; Faugeras, C.; Langbein, W.; Potemski, M.; Kasprzak, J. Radiatively Limited Dephasing and Exciton Dynamics in MoSe$_2$ Monolayers Revealed with Four-Wave Mixing Microscopy. *Nano Lett.* **2016**, *16*, 5333−5339.

(30) Singh, A.; Moody, G.; Tran, K.; Scott, M. E.; Overbeck, V.; Berghauser, G.; Schaibley, J.; Seifert, E. J.; Pleskot, D.; Gabor, N. M.; Yan, J. Q.; Mandrus, D. G.; Richter, M.; Malic, E.; Xu, X. D.; Li, X. Q. Trion Formation Dynamics in Monolayer Transition Metal Dichalcogenides. *Phys. Rev. B: Condens. Matter Mater. Phys.* **2016**, *93*, 041401.

(31) Berghaeuser, G.; Malic, E. Analytical Approach to Excitonic Properties of MoS$_2$. *Phys. Rev. B: Condens. Matter Mater. Phys.* **2014**, *89*, 125309.

(32) Ye, Z.; Cao, T.; O'Brien, K.; Zhu, H.; Yin, X.; Wang, Y.; Louie, S. G.; Zhang, X. Probing Excitonic Dark States in Single-Layer Tungsten Disulphide. *Nature* **2014**, *513*, 214−218.

(33) Chernikov, A.; van der Zande, A. M.; Hill, H. M.; Rigosi, A. F.; Velauthapillai, A.; Hone, J.; Heinz, T. F. Electrical Tuning of Exciton Binding Energies in Monolayer WS$_2$. *Phys. Rev. Lett.* **2015**, *115*, 126802.

(34) Sim, S.; Park, J.; Song, J.-G.; In, C.; Lee, Y.-S.; Kim, H.; Choi, H. Exciton Dynamics in Atomically Thin MoS$_2$: Interexcitonic Interaction and Broadening Kinetics. *Phys. Rev. B: Condens. Matter Mater. Phys.* **2013**, *88*, 075434.

(35) Mai, C.; Barrette, A.; Yu, Y.; Semenov, Y. G.; Kim, K. W.; Cao, L.; Gundogdu, K. Many-Body Effects in Valleytronics: Direct Measurement of Valley Lifetimes in Single-Layer MoS$_2$. *Nano Lett.* **2014**, *14*, 202−206.

(36) Carvalho, A.; Ribeiro, R. M.; Castro Neto, A. H. Band Nesting and the Optical Response of Two-Dimensional Semiconducting Transition Metal Dichalcogenides. *Phys. Rev. B: Condens. Matter Mater. Phys.* **2013**, *88*, 115205.

(37) Lupton, J. M. Single-Molecule Spectroscopy for Plastic Electronics: Materials Analysis from the Bottom-Up. *Adv. Mater.* **2010**, *22*, 1689−1721.

(38) van der Zande, A. M.; Huang, P. Y.; Chenet, D. A.; Berkelbach, T. C.; You, Y.; Lee, G.-H.; Heinz, T. F.; Reichman, D. R.; Muller, D. A.; Hone, J. C. Grains and Grain Boundaries in Highly Crystalline Monolayer Molybdenum Disulphide. *Nat. Mater.* **2013**, *12*, 554−561.

(39) Tongay, S.; Suh, J.; Ataca, C.; Fan, W.; Luce, A.; Kang, J. S.; Liu, J.; Ko, C.; Raghunathanan, R.; Zhou, J.; Ogletree, F.; Li, J.; Grossman, J. C.; Wu, J. Defects Activated Photoluminescence in Two-Dimensional Semiconductors: Interplay between Bound, Charged, and Free Excitons. *Sci. Rep.* **2013**, *3*, 2657.

(40) Sercombe, D.; Schwarz, S.; Del Pozo-Zamudio, O.; Liu, F.; Robinson, B. J.; Chekhovich, E. A.; Tartakovskii, I. I.; Kolosov, O.; Tartakovskii, A. I. Optical Investigation of the Natural Electron Doping in Thin MoS$_2$ Films Deposited on Dielectric Substrates. *Sci. Rep.* **2013**, *3*, 3489.

(41) Lin, Y.; Ling, X.; Yu, L.; Huang, S.; Hsu, A. L.; Lee, Y.-H.; Kong, J.; Dresselhaus, M. S.; Palacios, T. Dielectric Screening of Excitons and Trions in Single-Layer MoS$_2$. *Nano Lett.* **2014**, *14*, 5569−5576.

(42) Yang, F.; Wilkinson, M.; Austin, E. J.; Odonnell, K. P. Origin of the Stokes Shift - a Geometrical Model of Exciton Spectra in 2D Semiconductors. *Phys. Rev. Lett.* **1993**, *70*, 323−326.

(43) Gurioli, M.; Vinattieri, A.; Martinezpastor, J.; Colocci, M. Exciton Thermalization in Quantum-Well Structures. *Phys. Rev. B: Condens. Matter Mater. Phys.* **1994**, *50*, 11817−11826.

(44) Polimeni, A.; Patane, A.; Alessi, M. G.; Capizzi, M.; Martelli, F.; Bosacchi, A.; Franchi, S. Stokes Shift in Quantum Wells: Trapping *Versus* Thermalization. *Phys. Rev. B: Condens. Matter Mater. Phys.* **1996**, *54*, 16389−16392.

(45) Scheuschner, N.; Ochedowski, O.; Schleberger, M.; Maultzsch, J. Resonant Raman Profiles and μ-Photoluminescence of Atomically Thin Layers of Molybdenum Disulfide. *Phys. Status Solidi B* **2012**, *249*, 2644−2647.

(46) Ruckenstein, A. E.; Schmittrink, S. Many-Body Aspects of the Optical-Spectra of Bulk and Low-Dimensional Doped Semiconductors. *Phys. Rev. B: Condens. Matter Mater. Phys.* **1987**, *35*, 7551−7557.

(47) Liang, Y. F.; Yang, L. Carrier Plasmon Induced Nonlinear Band Gap Renormalization in Two-Dimensional Semiconductors. *Phys. Rev. Lett.* **2015**, *114*, 063001.

(48) Park, K.-D.; Khatib, O.; Kravtsov, V.; Clark, G.; Xu, X.; Raschke, M. B. Hybrid Tip-Enhanced Nanospectroscopy and Nanoimaging of Monolayer WSe$_2$ with Local Strain Control. *Nano Lett.* **2016**, *16*, 2621−2627.

(49) Perdew, J. P.; Burke, K.; Ernzerhof, M. Generalized Gradient Approximation Made Simple. *Phys. Rev. Lett.* **1996**, *77*, 3865−3868.

(50) Giannozzi, P.; Baroni, S.; Bonini, N.; Calandra, M.; Car, R.; Cavazzoni, C.; Ceresoli, D.; Chiarotti, G. L.; Cococcioni, M.; Dabo, I.; Dal Corso, A.; de Gironcoli, S.; Fabris, S.; Fratesi, G.; Gebauer, R.; Gerstmann, U.; Gougoussis, C.; Kokalj, A.; Lazzeri, M.; Martin-Samos, L.; Marzari, N.; Mauri, F.; Mazzarello, R.; Paolini, S.; Pasquarello, A.; Paulatto, L.; Sbraccia, C.; Scandolo, S.; Sclauzero, G.; Seitsonen, A. P.; Smogunov, A.; Umari, P.; Wentzcovitch, R. M. Quantum Espresso: A Modular and Open-Source Software Project for Quantum Simulations of Materials. *J. Phys.: Condens. Matter* **2009**, *21*, 395502.

(51) Hybertsen, M. S.; Louie, S. G. Electron Correlation in Semiconductors and Insulators: Band Gaps and Quasiparticle Energies. *Phys. Rev. B: Condens. Matter Mater. Phys.* **1986**, *34*, 5390–5413.

(52) Rohlfing, M.; Louie, S. G. Electron-Hole Excitations and Optical Spectra from First Principles. *Phys. Rev. B: Condens. Matter Mater. Phys.* **2000**, *62*, 4927–4944.

(53) Deslippe, J.; Samsonidze, G.; Strubbe, D. A.; Jain, M.; Cohen, M. L.; Louie, S. G. Berkeleygw: A Massively Parallel Computer Package for the Calculation of the Quasiparticle and Optical Properties of Materials and Nanostructures. *Comput. Phys. Commun.* **2012**, *183*, 1269–1289.